Feasibility study of a vision system for on-line monitoring of rolling contact fatigue tests

I Bodini[1], G Sansoni[2], M Lancini[1], S Pasinetti[2], and F Docchio[1]

[1]Dept. of Mechanical and Industrial Engineering, University of Brescia, via Branze, 38, 25123, Brescia, Italy
[2]Dept. of Information Engineering, University of Brescia, via Branze, 38, 25123, Brescia, Italy

ileana.bodini@unibs.it

Abstract. Wear and Rolling Contact Fatigue (RCF) tests on wheel/rail specimens are important to develop wheels of new materials for improved lifetime and performance, able to operate in harsh environments and at high rolling speeds. We have studied the feasibility of a novel non-invasive all-optical system, based on a high-speed video camera and two laser illumination sources, which is able to continuously monitor the dynamics of the specimens used to test wheel and rail materials, in a laboratory test bench. Surface micro- and macro-topography are monitored using blob analysis and 3D laser triangulation respectively. Blob analysis yields to good discrimination among the specimens, in terms of wear induced surface damage; the 3D measurement, which is characterized by a resolution of 0.033 mm, is able to monitor RCF effects.
The system is described with the aid of end-cycle specimens, as well as of intermediate specimens, prior to its installation in the test bench for rolling contact tests.

1. Introduction

Monitoring wheels and rails is important to increase safety in transportation [1, 2]. This can be done on-site, using different non-destructive inspection techniques such as electromagnetic tomography [3], axle box acceleration measurements [4], vision systems mounted on trains to detect rail conditions [5-7], and in laboratory, on test benches performing rolling contact fatigue tests [8-11].
Laboratory monitoring of damage in rolling contact can be effectively performed using optical techniques [12-16]. However, the rotation speeds of the specimens in current test benches, which is in the order of 500 rounds per minute (rpm), prevent the use of conventional photo cameras or video cameras without stopping the specimens, or at least without slowing them down, with the risk of altering the wear/fatigue process.
Recently, the use of high-speed video cameras, able to acquire images at very high frame-rate is becoming customary in a number of applications (from automotive, to industry, inspection, etc.). A recent paper [17] documents the use of these cameras to monitor a rolling-contact fatigue test for polymeric materials, illuminated by incoherent light. This approach is promising, since the high frame rate allows the monitoring of the specimens without reducing their speed, and without appreciable blurring, provided that the frame exposure is short enough, and, as a consequence, that the illumination is appropriate.
In addition to simple imaging with incoherent light, the use of lasers to monitor roughness as well as three-dimensional characteristics of surfaces is well known. In fact, the measurement of roughness (in

this case, generally related to wear effects) through diffuse scattering from the surface can be combined to the measurement of possible alterations of the 3D profiles of the specimen surface by means of suitable 3D techniques based on laser stripes [18]. Micro- and macro topological measurements can thus be effectively combined to the high-speed frame acquisition when a diffuse laser beam and a laser stripe are used as the illumination source for the specimen during the test, replacing incoherent light sources. The high laser brilliance makes these sources ideal also in the case of very short (tens of microseconds) exposure times.
In a companion Laboratory of our Department a detailed analysis of rolling contact fatigue on wheel-rail pairs is underway, in the framework of an industrial research aimed at improving the wheel performance and lifetime [19-22]. Dry and wet tests are conducted to simulate the different environmental conditions for train transportation. To further improve the test bench, the development of an on-line vision-based apparatus, able to work at a convenient distance from the test bench, and at variable specimen speeds, was requested.
This paper reports the results of a feasibility study carried out on a laboratory prototype based on a high-speed video camera for the wear monitoring of disk shaped specimens. In this activity, special care has been devoted to the design of efficient illumination and of dedicated processing procedures for the monitoring of the surface variations due to both wear and contact rolling fatigue (RCF) damages.

2. Experimental set-up

2.1. Optical layout of the system

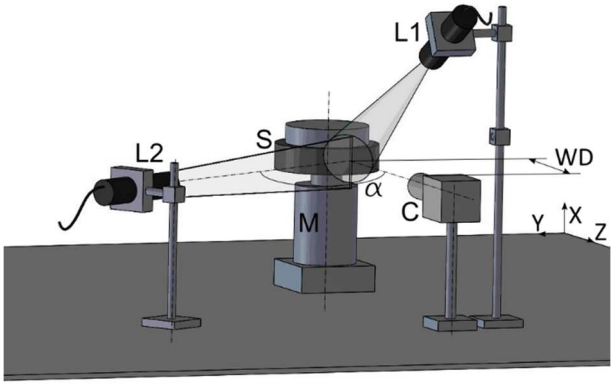

Figure 1. Layout of the laboratory experimental set-up. S: specimen, M: motor, C: high-speed camera, L1: defocused laser, L2: 3D laser stripe.

The schematic layout of the vision system for the cyclic contact experiments is depicted in Figure 1. The measurement target is a disk-shaped specimen S, fixed to the axle of a stepper motor M (HY200 2220 0100 AX08 – SCT Servo Control Technology), with a step angle of 1.80° ± 0.09°. The specimen can rotate at variable speeds up to f_s= 500 rpm, corresponding to 8.3 Hz. The heart of the observation system is the high-speed camera C (PROMON 501 – AOS Technologies AG), which can operate at increasing frame rates (f_c), by correspondingly decreasing the frame area. As an example, at 85 fps maximum frame area is (2048 × 1088) px, whereas at 3391 fps, it is reduced to (320 × 96) px. The exposure time is software-adjustable from 13 μs to the reciprocal of the camera acquisition frequency. To ensure optimal acquisition of the specimens under the operating rotational speed of 500 rpm, the frame rate is set at f_c = 377 fps, with an exposure time equal to 40 μs. The corresponding image resolution is (1280 × 240) px. The camera is equipped with a f/50 mm lens, and placed at a working distance WD of 300 mm from the specimen. The field of view is 26 mm along the X coordinate and 5 mm along the Y coordinate and the resulting spatial resolutions are Rs_X = 0.020 mm/px and

Rs_Y = 0.021 mm/px. At the image plane, X and Y are parallel to the image rows and columns respectively.

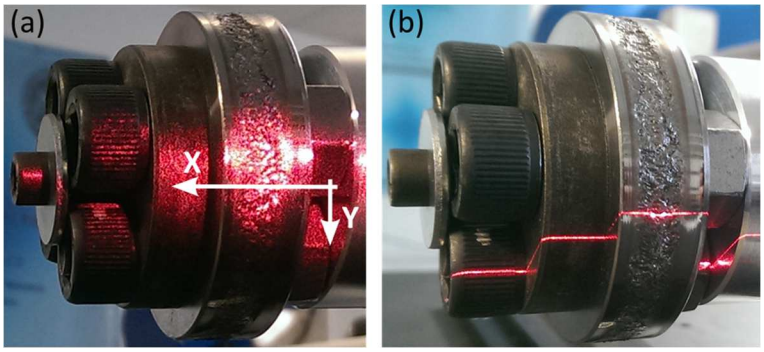

Figure 2. System illumination: (a) pattern projected by source L1, (b) pattern projected by source L2. The space coordinates X and Y are shown.

The camera can operate in free-running mode: the frame acquisition runs freely, and all the acquired frames are stored in a cyclic buffer within the Hard Disk of the PC. When the buffer is full, any new frame is inserted in, at the expense of the oldest acquired frame. The camera can also work in the trigger mode: in the event of a trigger signal, the camera stores the event together with the recorded frames.

2.2. The illumination sources

Monitoring the surface of rotating specimens at high speeds requires very low exposure times, to avoid image blurring. At speeds of 500 rpm, the exposure time is set equal to 40 μs. To enhance the visibility of the surface features, coherent light source is used: the high laser brilliance, combined with the possibility of shaping the irradiated areas, allows us to obtain suitable illumination of the specimens for all measurement purposes.

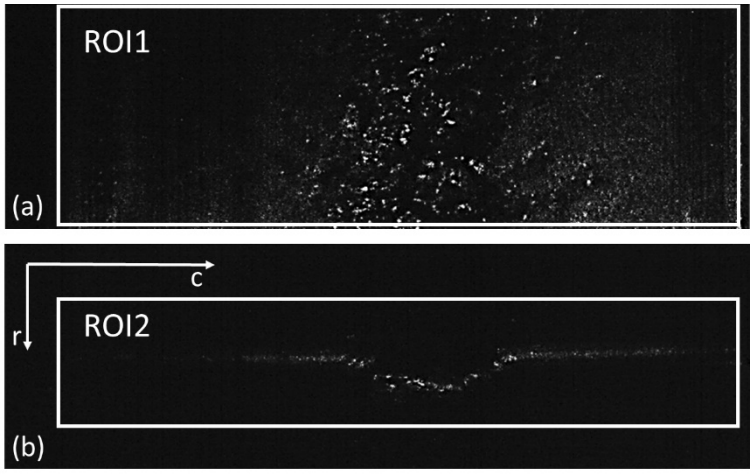

Figure 3. Acquired images from the laser sources. (a) Diffused light from L1 (frame ROI1); (b) Deformed light pattern from L2 (frame ROI2). Parameters r and c correspond to image rows and columns respectively.

In the presented system, two semiconductor laser modules (Lasiris™ SNF Laser), emitting 10 mW at 670 nm, have been assembled: they are denoted as L1 and L2 in Figure 1. The illumination pattern of

each source is shown in Figure 2; the corresponding acquired images are visible in Figure 3. Laser L1 projects a suitably defocused beam onto the specimen surface (Figure 2.a), and the scattered light carries information about the surface dips and crests (Figure 3.a) related to the spalling of the material, due to wear and fatigue effects. Laser L2 is equipped with a cylindrical lens that projects a line pattern (Figure 2.b), and that is mounted at an angle α of about 60° with respect to the camera optical axis. The aim is to capture the shape of the pattern induced by possible surface damages (Figure 3.b), due to rolling contact fatigue effects.
The image areas framed in Figure 3 correspond to specific regions of interest (ROIs) where dedicated processing is performed. The elaboration approach chosen for ROI1 is a 2D image processing based on blob analysis [24], while that ROI2 is a 3D image processing based on triangulation [25].

3. 2D-surface analysis

Groups of connected pixels within a closed boundary define a blob: we thought reasonable to argue that the position, number and dimension of these blobs could be directly correlated to wear- or fatigue-induced small surface dips, which lead to non-uniform backscattering of the light diffused by L1.

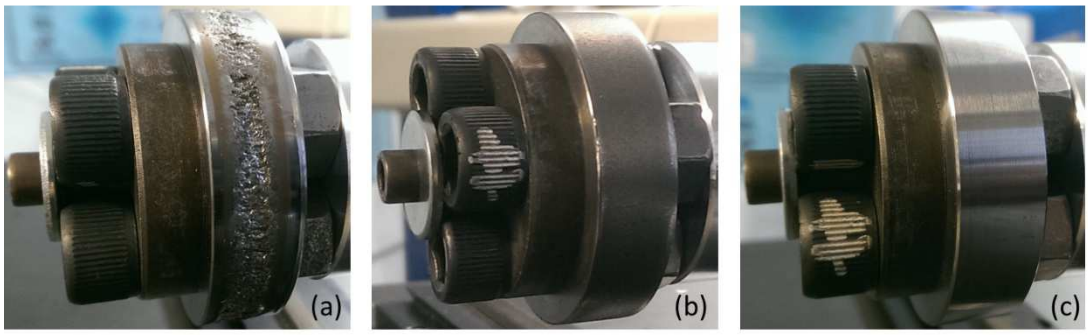

Figure 4. Samples representative of the different surfaces studied: (a) specimen ‘A’, (b) specimen ‘B’; and (c) specimen ‘C’.

To verify this hypothesis, the specimens shown in Figure 4 have been considered. The first one (specimen ‘A’) is a ‘post-mortem’ sample, made of rail steel UIC 900 A, which rolled 800 kcycles against a specimen made of Superlos® in a lubricated rolling contact fatigue test. The surface presents a serious damage, with dips and crests due to both wear and RCF effects. The second one (specimen ‘B’) is a specimen made of rail steel UIC 900 A, and has rolled 800 kcycles against a specimen made of ER8; the surface is more uniform than the one in Figure 4.a, but exhibits a certain level of roughness. The third one (specimen ‘C’) is made of rail steel UIC 900 A, before being tested on the cyclic contact tests, i.e., in the absence of surface damage.

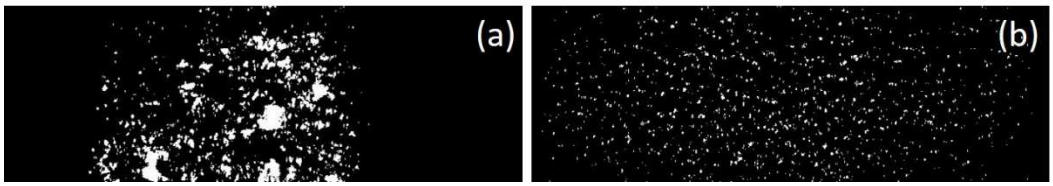

Figure 5. Example of the elaboration based on blob analysis carried out on specimens ‘A’ and ‘B’: (a) blobs detected on the ROI1 on specimen A; (b) blobs detected on the ROI1 of specimen B.

Figure 5 shows the results of the elaboration performed on the corresponding ROI1s of samples ‘A’ and ‘B’. Blobs have been obtained after suitable thresholding, to binarize images. The processing has been performed in the LabVIEW™ environment, using the NI IMAQ Vision suite of functions. The threshold has been set to 100 (on 8-bit black/white images).

In specimen 'A' (Figure 5.a), the blobs are concentrated in a confined region of the ROI, and their position reflects the topology of the surface damage, which is localized in the central part of the sample, where the contact between specimens takes place. In specimen 'B' (Figure 5.b), the blobs are uniformly located over the whole ROI, according to the fact that, in this sample, the wear process has increased the surface roughness, without localized material spalling. In addition, the two images differ in both the number and the area of the blobs. The blob analysis performed on the surface of the specimen C (not shown) reveals very few small blobs in accordance to the fact that the surface has not yet been subjected to any wear.

Based on these observations, the following parameters have been considered in the analysis: the blob density, the dispersion of the blob centres of gravity and the average blob area. For each analysed frame, the blob density is defined as follows:

$$\mathbf{d_B = N_B/A_1} \quad \textbf{(1)}$$

where N_B is the number of the blobs detected in ROI1 and A_1 is the area of ROI1 (in pixels).

The dispersion of the blob centres of gravity is defined as follows:

$$\mathbf{s_{xf} = ST.DEV}\left\{\boldsymbol{B^i}\right\}_{\boldsymbol{c}} \quad \textbf{(2)}$$

where $\{B^i\}_c$ represents the row coordinate of the center of gravity for each i^{th} blob belonging to column c, and ST.DEV$\{B^i\}_c$ is the standard deviation of the $\{B^i\}_c$ values with respect to the image columns.

The average blob area is calculated using the following formula:

$$\boldsymbol{a_B} = \frac{\mathbf{1}}{\boldsymbol{N_B}} \sum_{\boldsymbol{i=1}}^{\boldsymbol{N_B}} \boldsymbol{a_i} \quad \textbf{(3)}$$

where a_i is the area of each blob in the image. The values calculated for d_B, s_{xf} and a_B for specimens 'A', 'B' and 'C' are shown in Table 1. Here, the maximum values of both d_B and s_{xf} are observed in specimen 'B' according to the fact that N_B is higher than for specimen 'A' and 'C' and that the blobs are present over the whole ROI, which is confirmed by Figure 5.b. The value of a_B in specimen 'A' reflects the fact that the blobs area span a wide range, resulting into high values of both the average value and the standard deviation.

Besides the above parameters, the following index has been also defined:

$$\boldsymbol{r_B} = \frac{\sum_{\boldsymbol{i=1}}^{\boldsymbol{N_B}} \boldsymbol{a_i}}{\boldsymbol{A_1}} \quad \textbf{(4)}$$

Parameter r_B represents the ratio between the image area occupied by the blobs and the total area of ROI1 and is an estimation of the damage ratio. For specimens 'A', 'B' and 'C' the values of r_B are 6.9 %, 2.6 % and 0.0024 %, respectively.

Seven specimens have been tested for 2D surface analysis: all them are made of the same rail steel UIC 900 A, and have been tested for the same number of cycles (800 k). They only differ for the type of rolling contact fatigue test (dry or wet/lubricated), and, when the type of test is the same, for the type of counter-rolling wheel steel in the test. For each specimen, a 2 s video has been recorded, and each frame has been elaborated.

Following completion of the processing of the temporal frame sequence, the average values of the above parameters over all frames, i.e. D_B, S_X, A_B and R_B are calculated.

Table 1. The values of d_B, s_{xf} and a_B in specimens 'A', 'B' and 'C'.

	d_B [px^{-1}]	s_{xf} [px]	a_B [px]
specimen 'A'	2.9×10^{-3}	100.7	24.2 ± 80.4
specimen 'B'	4.9×10^{-3}	165.0	5.3 ± 4.2
specimen 'C'	1.2×10^{-5}	5.7	2

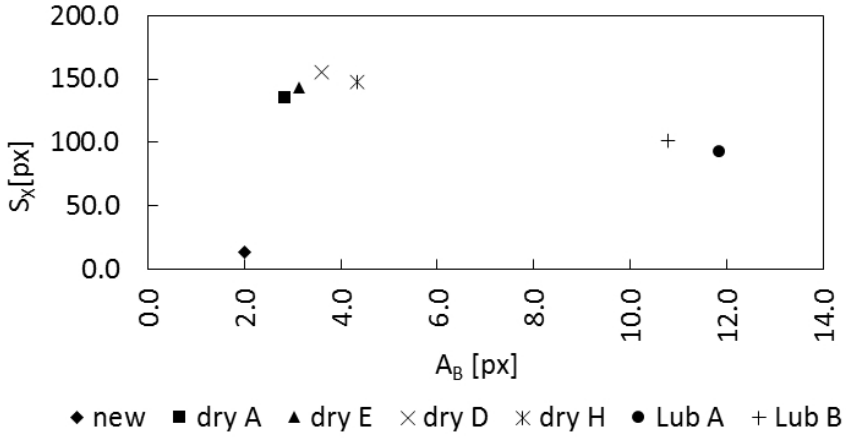

Figure 6. Blob dispersion S_X *vs* the single blob average area A_B.

Figure 6 shows a plot of the blob dispersion S_X *vs* the average blob area A_B for all the tested specimens. Each point in the graph represents a different specimen: 'new' is specimen 'C' in Figure 4.c; 'Lub A' underwent a wet test and rolled against a wheel made of ER8; 'Lub B' is the specimen 'A' in Figure 4.a; 'dry A' and 'dry H' underwent dry tests and rolled against wheels made of ER8; 'dry D' and 'dry E', underwent dry tests and rolled against wheels made of Superlos®. From Figure 6 it is evident that 'new' exhibits small values of both A_B and S_x. All the 'dry' specimens exhibit small average blob areas (between 3 and 5 px), but with markedly higher blob dispersion (about 150 px). The LubA and LubB specimens are both characterized by values of A_B between 10 and 12 px, and S_X values of about 100 px.

The observation of the plot in Figure 6 highlights that new specimens, 'dry' and lubricated ones, are all well separated from each other. This result is in accordance with the literature which shows that wear effects are dominant in dry tests, while fatigue effects are dominant in lubricated tests [19, 22, 23].

Figure 7 shows a plot of the density of blobs D_B *vs* the average blob area A_B for all the tested specimens. Here, specimens that underwent a dry test are clearly separated from the ones that underwent a lubricated test, principally thanks to very different values of A_B, while, for what concerns D_B, the two types of specimens overlap. In particular, for 'dry' specimens the density of blobs assumes different values, from 500 px^{-1} to 2000 px^{-1}, while the 'lubricated' ones show only high values of D_B, included between 1500 px^{-1} and 2000 px^{-1}. As expected, the new specimen is characterized by a value of D_B very close to zero, and is therefore distinguishable from 'dry' and 'lubricated' ones.

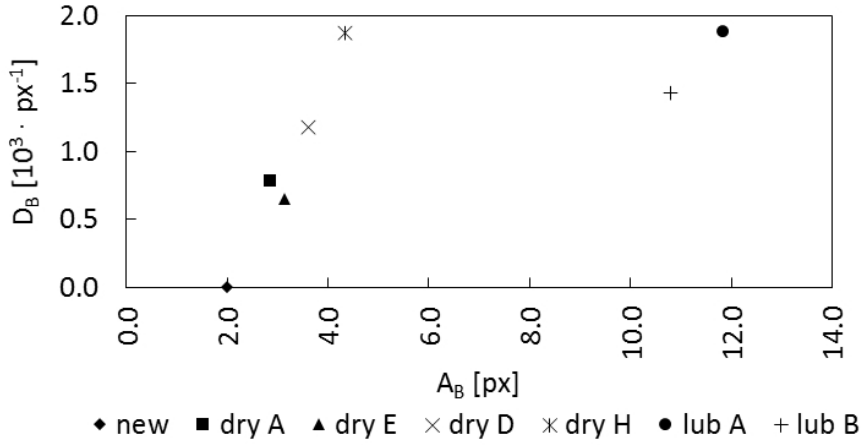

Figure 7. Density of blobs D_B *vs* the single blob average area A_B.

By Figure 6 and Figure 7, it appears that A_B and S_x are suitable indexes to distinguish between new specimens and different types of surface damage, while DB is a more variable quantity and does not unambiguously identify a single type of specimen.

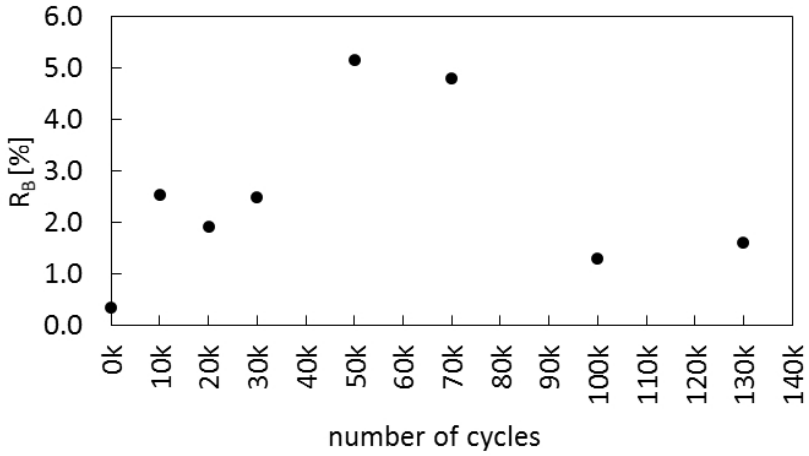

Figure 8. Time evolution of the damage ratio R_B.

The system has also been characterized in relation to its ability to monitor the temporal evolution of specific specimens during dry rolling contact fatigue tests. In particular, a specimen made of ER8 has been monitored by acquiring videos after pre-defined numbers of cycles. Figure 8 shows the time evolution of the area ratio R_B *vs* the number of cycles. R_B increases rapidly after 10 kcycles, remains fairly constant up to 30 kcycles. It increases further after 50 kcycles, until 70 kcycles. Finally, after 100 kcycles, R_B decreases. This result is in accordance with the research presented in [23], in which RCF tests have been performed to study how RCF and wear proceed and interact. These results confirm that wear is a concurrent phenomenon, which removes material layers from the surface and consequently affect ratchetting evolution. In particular, wear has a role in stabilizing the strain field for a high number of cycles, and prevents long crack formation. This is also supported by Figure 8, which shows how the damage ratio R_B for a higher number of cycles is lower than for an intermediate number of cycles.

4. 3D surface analysis

4.1. The 3D measurement performed on ROI2

The aim of this procedure is to retrieve the depth of a deformation of the surface in correspondence of the points illuminated by laser L in Figure 9, which correspond to L2 in Figure 1. This measurement has been thought to be of interest, especially in combination with the 2D description of the specimen resulting from the blob analysis. Optical triangulation has been used to perform this task. The principle is well known, and can be easily understood by looking at the geometry shown in Figure 9. Here, points L and C are the exit and the entrance pupils of the laser and the camera optics respectively. Considering a surface point A, its conjugate at the camera plane is A'. The variation along the depth coordinate Z is represented by distance h: the laser ray $\overline{LA}$ impinges the surface at point B, which is imaged at point B' at the image plane. The relationship between the depth variation h and the ray shift $y' = \overline{A'B'}$ is obtained considering that triangles $\widehat{BAD}$ and $\widehat{CAL}$ are similar, hence the following relationship holds:

$$\frac{y}{h} = \frac{d}{s} \tag{5}$$

where $y = \overline{DB}$ and $d = \overline{CL}$.

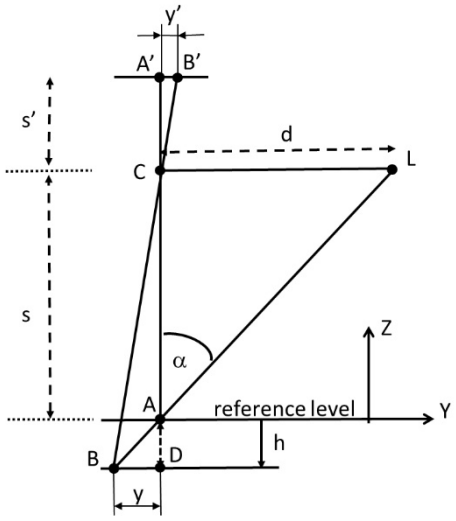

Figure 9. Optical geometry of the 3D measurement approach.

In addition, the relationship between y and y' is as follows:

$$\frac{y'}{y} = \frac{s'}{s-h} \tag{6}$$

where *h* can be a negative number.
Combining Eq. (5) and Eq. (6), and solving for *h*, we obtain the following formula:

$$h = \frac{s^2 \cdot y'}{d \cdot s' + y' \cdot s} \tag{8}$$

Eq. (8) states that, by measuring the deformation *y'* along Y of the line profile, it is possible to estimate the surface depth along the Z coordinate (provided that parameters s, *s'* and *d* are known). Values *y'* can be measured by evaluating, for each image column of index *c*, the centre of gravity of the corresponding grey levels $\{l_r\}$ by means of the following relation:

$$b_c = \frac{\sum_r l_r \cdot r}{\sum_r l_r} \tag{9}$$

As an example, Figure 10 shows the result of this procedure when applied to the grey level values shown in Figure 3.b: each point represents a centre of gravity of coordinates (c, b_c). By multiplying each value b_c by the pixel size, the corresponding y' value is obtained (in mm). The estimate of parameters *s*, *s'* and *d* has been performed by means of a suitable calibration procedure, that is presented in the following Section 4.2.

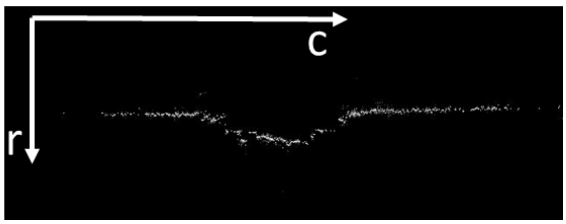

Figure 10. Row-shift at each column of the image in Figure 3.b

4.2. Procedure for estimating the 3D measurement parameters
The estimation of parameters *s*, *s'* and *d* has been accomplished as follows. Solving Eq. (8) for parameter *y'* we obtain:

$$y' = \frac{h \cdot s' \cdot d}{s(s-h)} \tag{10}$$

In Eq. (10), *s* and *s'* are linked by the well-known Gaussian formula:

$$\frac{1}{s} + \frac{1}{s'} = \frac{1}{f} \tag{11}$$

or:

$$s' = \frac{s \cdot f}{s-f} \tag{12}$$

where *f* is the focal length. Looking at Figure 9, *d* can be derived as:

$$d = s \cdot tg(\alpha) \tag{13}$$

Substituting (11) and (12) in (10), the following relation is obtained:

$$y' = \frac{h \cdot f \cdot s \cdot tg(\alpha)}{(s-h) \cdot (s-f)} \tag{14}$$

Eq. (14) has been used to estimate parameter *s*. To this aim, a plane calibration master has been oriented parallel to plane XY, and has been moved at known positions $\{h_n\}$ along –Z, using a sliding table with a resolution of 0.01 mm, over a range of 2.7 mm. The value h_0 has been set to correspond to the position of point A in Figure 9. At each position *n*, the laser pattern projected by L2 has been acquired. Using Eq. (9), the centres of gravity $\{(c, b_c)\}_n$ have been estimated with sub-pixel accuracy; the corresponding values $\{y'\}_n$ have been computed, and their average $E[\{y'\}_n]$ over the image columns has been taken as a value representative of the profile position at distance h_n.

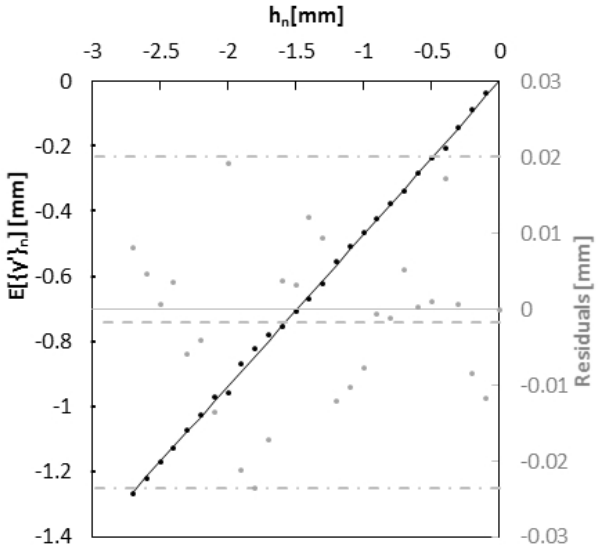

Figure 11. Calibration curve of the 3D laser slit.

Using Eq. (14) for different $(E[\{y'\}_n]\text{-}h_n)$ pairs, and at known values of focal length *f* and of angle α, led to the estimate of parameter *s* equal to 226.30 mm, using a least square method with an overall standard uncertainty of the model equal to 0.011 mm. From Eq. (12) we obtained *s'* = 64.18 mm and using Eq. (10) we evaluated *d* = 376.63 mm.

The curve shown in Figure 11 plots the relationship between $E[\{y'\}_n]$ and h_n. Black symbols (left vertical axis) represent the set of $(E[\{y'\}_n]\text{-}h_n)$ couples; their interpolation (continuous line) is well approximated by a straight line, which is expected when considering that, in Eq. (10), $h << s$. Symbols in grey (right vertical axis), represent the residuals, i.e. the differences between experimental points

$E[\{y'\}_n]$ and interpolated ones at each h_n value. Their distribution along Z turns to be compatible with zero, with a correlation coefficient of 0.0045, demonstrating that the residuals are stochastically distributed.

4.3. System performance

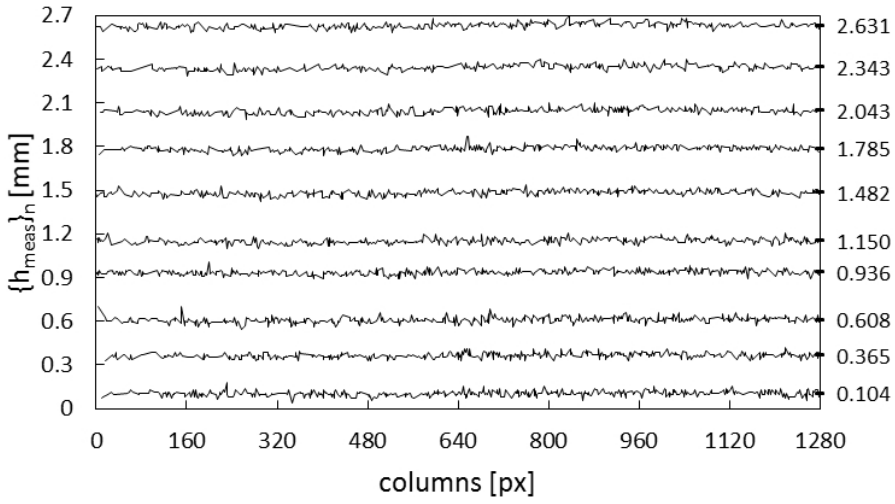

Figure 12. Values of h measured along the image columns for known positions h_n.

A number of experiments have been carried out to test the 3D measurement. First, the values obtained for parameters *s*, s' and *d* by means of the calibration described in Section 4.2 have been used in Eq. (8), to estimate the quality of the measurement. To this aim, a master plane has been positioned along the measurement interval at steps of 0.1 mm, and new images have been acquired and elaborated by using the triangulation formula of Eq. (8). As an example, Figure 12 presents the plots of measured values $\{h_{meas}\}_n$ along the image columns at each known position h_n for a starting value of n equal to 0 mm up to 2.7 mm at steps of 0.3 mm. The average value $E[\{h_{meas}\}_n]$ calculated for each $\{h_{meas}\}_n$ signal is also reported (right axis).

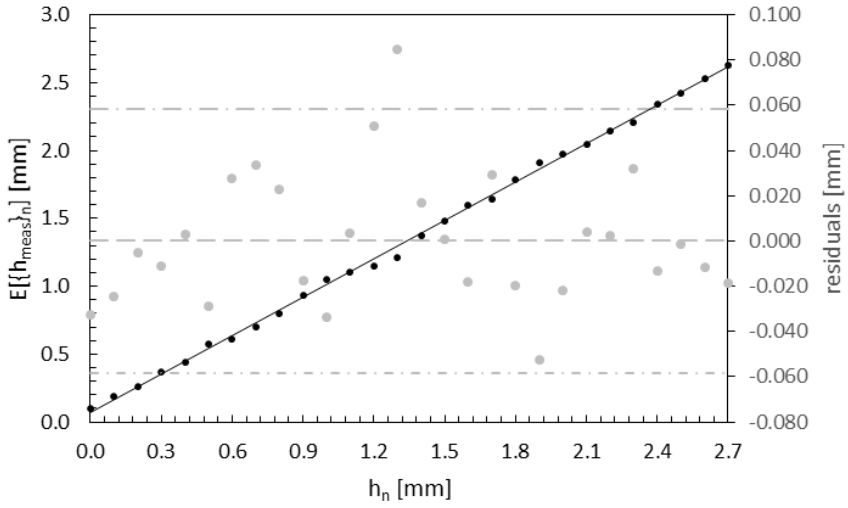

Figure 13. Plot of the average $E[\{h_{meas}\}_n]$ of measured values $\{h_{meas}\}_n$ vs known positions h_n.

Values $E[\{h_{meas}\}_n]$ are plotted *vs* values h_n in Figure 13 (black dots). The linear interpolation results into an angular coefficient of (0.9542 ± 0.0075), with a linear correlation coefficient of 0.999. Along the right vertical axis, in grey, the residuals are presented. Their average value is compatible with zero and the corresponding linear coefficient is equal to 0.33, which demonstrate a stochastic distribution of the residuals.

An example of the measurement performed on specimen 'B' of Figure 4.b is reported in Figure 14.a: the stripe projected by the laser source L2 is visible on the surface of the specimen. Figure 14.b shows the image acquired while the specimen was rotating at fs=500 rpm; the resulting measurements are shown in Figure 14.c.

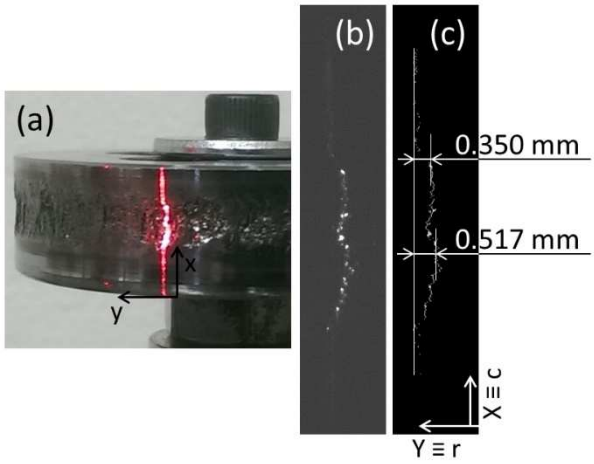

Figure 14. Example of a 3D measurement, performed on images acquired at a speed of 377 fps. (a) the line profile projected on the specimen surface; (b) the corresponding image of the deformed line profile; (c) measured values $\{h_{meas}\}_n$ along the image columns (X coordinate).

5. Conclusions

We have demonstrated the feasibility of a novel set-up for the on-line monitoring of rolling contact fatigue tests on wheel/rail specimens, based on a high-speed camera and on two laser sources, able to perform micro- and 3D macro-profile measurements, as well as angular position measurements. A prototype has been realized and its performances studied. The system is now installed in the test bench for rolling contact fatigue tests and is yields new information about the different types of damages, such as wear and fatigue, and the behaviour of different materials during the whole lifetime of the specimens.

6. References

[1] D. F. Cannon, K. O. Edel, S. L. Grassie, and K. Sawley 2003 *Fatigue Fract. Eng.M.* **26** 865.
[2] U. Zerbst, and S. Beretta 2011 *Eng. Fail. Anal.* **18** 534.
[3] Z. Liu, W. Li, F. Xue, J. Xiafang, B. Bu, and Z. Yi 2015 *IEEE Trans. Magn.* **51** 6201907
[4] Z. Li, M. Molodova, A. Núñez, and R. Dollevoet 2015 *IEEE Trans. Ind. Electron.* **62** 4385
[5] Z. Liu, F. Li, B. Huang, and G. Zhang 2014 *J. Opt. Soc. Am. A* **31** 1721
[6] Q. Li, and S. Ren 2012 *IEEE Trans. Instrum. Meas.* **61** 2189
[7] L. Jie, L. Siwei, L. Qingyong, Z. Hanqing, and R. Shengwei 2009 *IEEE International Symposium on Industrial Electronics (Seoul)* p 769
[8] U. Olofsson, and T. Telliskivi 2003 *Wear* **254** 80
[9] G. Zhou, C. He, G. Wen, and Q. Liu 2015 *Tribol. Int.* **91** 160
[10] C. Kammerhofer, A. Hohenwarter, and R. Pippan 2014 *Wear* **316** 101

[11] D. I. Fletcher, and S. Lewis 2013 *Wear* **298-299** 57
[12] J. Zhang, M. Korsten, and P. Regtien 2003 *Proc. XVII IMEKO World Congress (Dubrovnik*) p 1960
[13] G. A. Al-Kindi, and B. Shirinzadeh 2007 *Int. J. Mach. Tool. Manu.* **47** 697
[14] E. Kayahan, H. Oktem, F. Hacizade, H. Nasibov, and O. Gunogdu 2010 *Tribol. Int.* **43** 307
[15] Y-K. Fuh, K. C. Hsu, and J. R. Fan 2012 *Opt. Laser Eng.* **50** 312
[16] Z. Gao, and X. Zhao 2012 *Opt. Laser Eng.* **50** 668
[17] J. Sukuraman, S. Soleimani, P. De Baets, V. Rodriguez, K. Douterloigne, W. Philips, and M. Ando 2012 *Wear* **296** 702
[18] G. Sansoni, P. Bellandi, and F. Docchio 2011 *Meas. Sci. Technol.* **22** 075302
[19] A. Mazzù, C. Petrogalli, and M. Faccoli 2015 *Wear* **322-323** 181
[20] M. Lancini, I. Bodini, D. Vetturi, S. Pasinetti, A. Mazzù, L. Solazzi, C. Petrogalli, and M. Faccoli 2015 *ACTA IMEKO* **4** 66
[21] A. Mazzù, L. Solazzi, M. Lancini, C. Petrogalli, A. Ghidini, and M. Faccoli 2015 *Wear* **342-343** 22
[22] G. Donzella, M. Faccoli, A. Ghidini, A. Mazzù, and R. Roberti 2005 *Eng. Fract. Mec.* **72** 287
[23] G. Donzella, M. Faccoli, A. Mazzù, C. Petrogalli, and R. Roberti 2011 *Wear* **271** 408
[24] T. B. Moeslund 2012 BLOB Analysis *Introduction to video and image processing – Building real systems and applications* ed. Undergraduate topics in computer science (London: Springer Verlag) pp 103 – 116
[25] G. Sansoni, M. Trebeschi, F. Docchio 2009 *Sensors* **9** 568

Acknowledgments
We acknowledge the invaluable assistance of Prof. A. Mazzù, Dr. M. Faccoli and Dr. C. Petrogalli in the preparation of the specimens, and in the design of the experiments. We are also very grateful to Lucchini RS – Italy, that provided material and technical support, and wish to thank Mr. S. Bonometti, Mr. B. Tratta and Mr. G. Coffetti for their support in the experimental activities.